Quantum Characterization of Single Photon Detectors

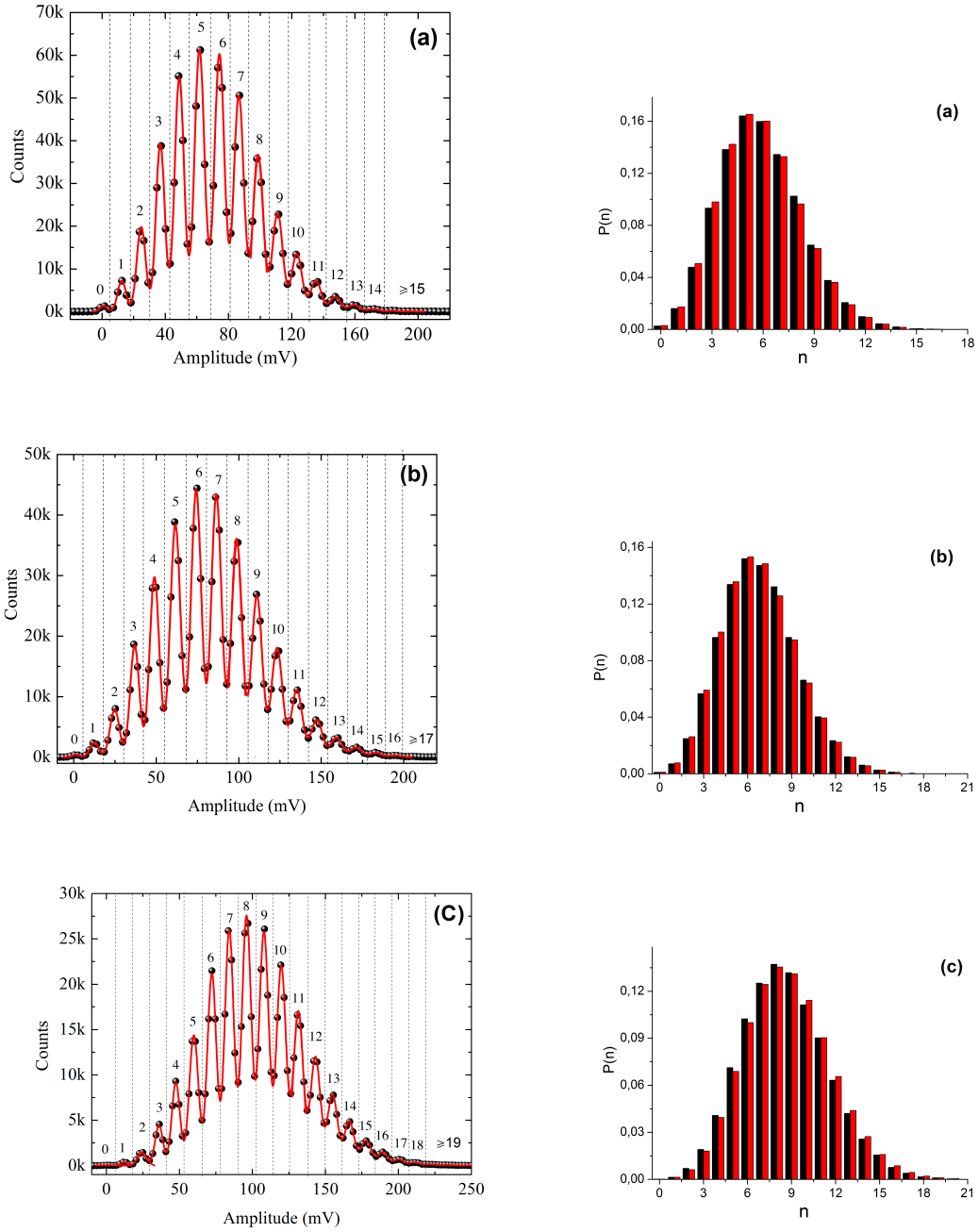

Figure 4.5: In the graphs on the left, dots represent TES counts, solid lines are the Gaussian fits on the experimental data, and the dotted vertical lines are the thresholds. In the plots on the right, the experimental probability distribution (black bars) is compared with the corresponding Poisson distribution of mean value $\eta\mu$ (with $\eta = 6,70\%$) (red bars). Graphs (a), (b) and (c) are obtained with a coherent state characterized by a mean photon number per pulse $\mu = 87$, $\mu = 101$ and $\mu = 130$ respectively. The fidelities obtained in cases (a), (b) and (c) are $99,98\%$, $99,95\%$ and $99,97\%$ respectively.

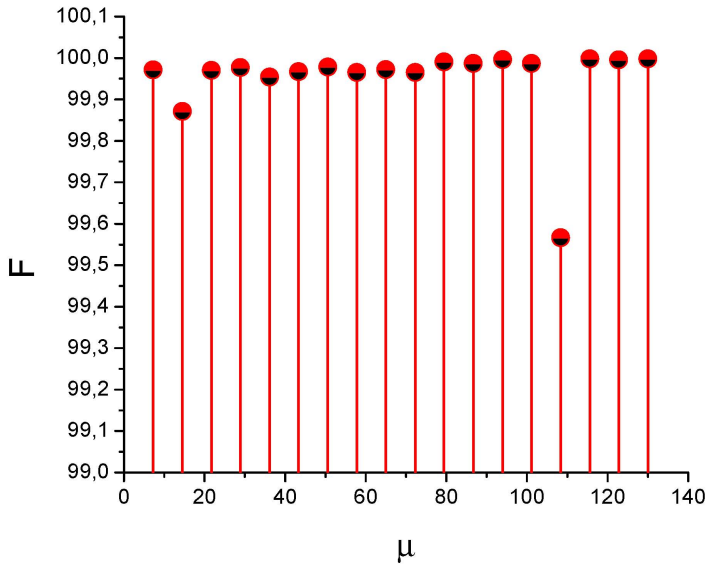

Figure 4.6: Fidelity between the experimental probability distribution $p(n, j)$ and a Poisson distribution of mean value $\eta\nu$ (with $\eta = 6,70\%$), for the different states $|\alpha_j\rangle$ with mean photon number per pulse μ_j. Fidelities higher than $99,5\%$ for all the input states are a confirmation of an excellent agreement between experimental results and theoretical predictions.

of the ideal photon number spectral measure with

$$B_{nm} = \begin{pmatrix} m \\ n \end{pmatrix} \eta^n (1-\eta)^{m-n} \tag{4.6}$$

where η is the quantum efficiency of the detector.

In order to compare the POVM elements B_{nm} of the linear detector with the reconstructed POVM elements Π_{nm}, we have to first estimate the value of the quantum efficiency η. This can be done on the sole basis of the experimental data using ML estimation, i.e. we average the values of η which maximize the log-likelihood functions

$$L_j = \sum_n N_{nj} \log \left(\sum_m B_{nm} q_{mj} \right) \tag{4.7}$$

where N_{nj} is the number of n-count events obtained with the j^{th} input state $|\alpha_j\rangle$.

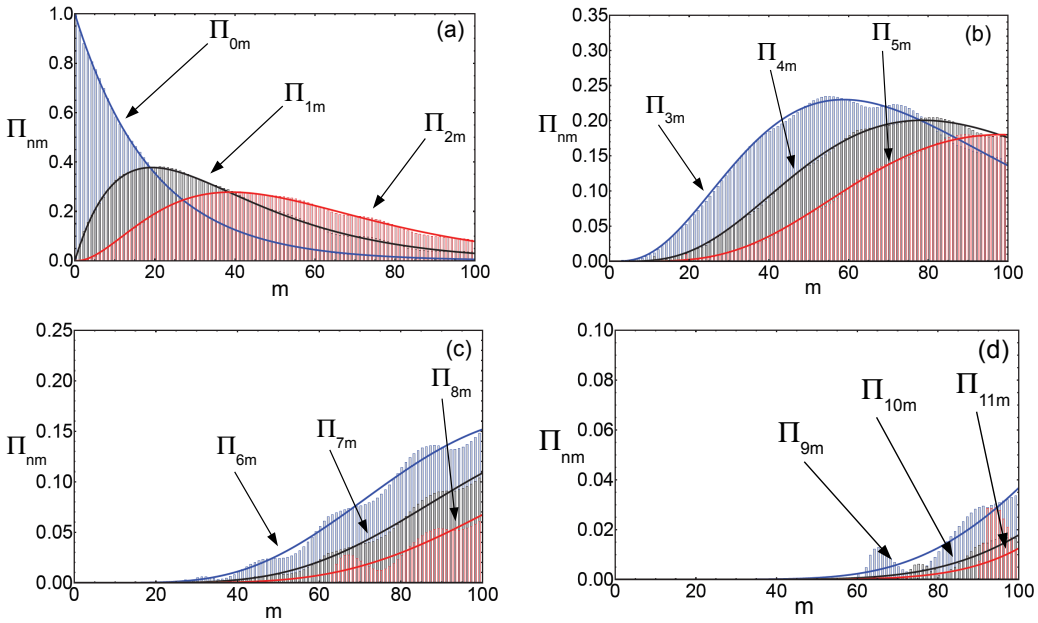

Figure 4.7: Reconstruction of the POVM of our TES photon couinting system. Continuous lines represent the POVM elements of a linear photon counter with quantum efficiency $\eta = 6,70\%$. Histograms show the matrix elements Π_{nm} as a function of $m = 0, ..., 100$ for (a) $n = 0, 1, 2$, (b) $n = 3, 4, 5$, (c) $n = 6, 7, 8$ and (d) $n = 9, 10, 11$.

For each signal probe the value of an η_j is estimated and the value of η is given by the average over the ensemble. The overall procedure leads to an estimated value of the quantum efficiency $\eta = (6,70 \pm 0,04)\%$, where the uncertainty accounts for the statistical fluctuations.

As shown in Figure 4.7, an excellent agreement between the reconstructed POVM and the one expected from a linear photon counter with the estimated quantum efficiency is obtained. In particular, for $m \lesssim 100$ the elements of the POVM are reliably reconstructed, while the quality of the reconstruction degrades for values of $m \gtrsim 100$. As shown in Figure 4.8, the fidelity $F_m = \sum_n \sqrt{\Pi_{nm} B_{nm}}$ is larger than 99% in the regime $m \leq 100$, whereas it degrades to 95% for $100 \leq m \leq 140$. The effects of the experimental uncertainties are investigated by performing a sensitivity analysis taking into account the uncertainties on the energy of the input state and on the attenuators obtaining, for the twelve entries, fidelities greater than $98,35\%$.

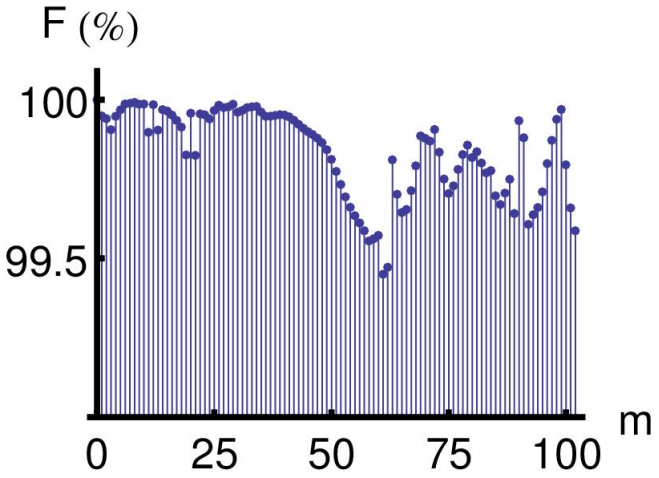

Figure 4.8: Fidelity between the reconstructed POVM elements at fixed m and those of a linear photon counter with quantum efficiency $\eta = 6,70\%$. Values of F larger than $99,5\%$ for $m \leqslant 100$ are the evidence of the reliability of the reconstruction.

The measured distributions $p(n,j)$ are compared with those obtained for a linear detector, $l(n,j)$, and with those obtained using the reconstructed POVM elements, $r(n,j)$, with the aim to further confirm the linearity hypothesis, as well as to assess the reliability of the reconstruction. The expression for the distribution of a linear detector is

$$l(n,j) = \eta^n e^{-\eta\mu_j} \frac{\mu_j^n}{n!} \tag{4.8}$$

while the distribution expression using the reconstructed Π_{nm} is

$$r(n,j) = \sum_{m=n}^{M} \Pi_{nm} q_{mj}. \tag{4.9}$$

The three distributions for the whole set of probing coherent states are reported in Figure 4.9. The absolute differences between te measured distribution and the distributions of Eqs. (4.8) and (4.9), $|p(n,j) - l(n,j)|$ and $|p(n,j) - r(n,j)|$, are shown in Figure 4.10. As is apparent from the plots, the different determinations of the distributions are in excellent agreement. This confirms the linear behaviour of the detector, and proves that the reconstructed POVM provides a reliable description of the detection process.

To take into account the possible presence of dark counts, the detection model was

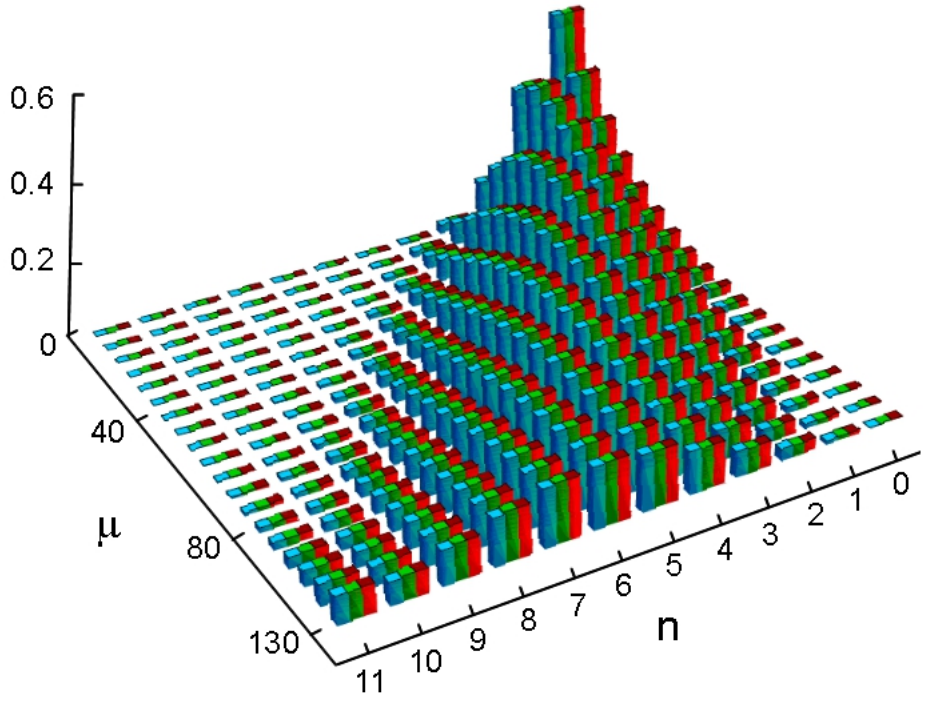

Figure 4.9: Comparison of the measured distributions $p(n, j)$ (blue bars on the left of each group) of the coherent state $|\alpha_j\rangle$ used for the POVM reconstruction, with those obtained using the reconstructed POVM elements $r(n, j)$ (green central bars) and with those obtained under the linear hypothesis $l(n, j)$ (red right bars).

modified: in this case, upon assuming a Poissonian background, the matrix elements of the POVM are given by

$$\Pi_{nm} = e^{-\gamma} \sum_j \frac{\gamma^j}{j!} B_{(n-j)m}. \tag{4.10}$$

A ML procedure is developed to estimate both the quantum efficiency η and the mean number of dark counts per pulse γ. The value of η found with this procedure is statistically indistinguishable from the one obtained with the linear-detector model. The estimated dark counts per pulse are $\gamma = (-0,03 \pm 0,04)$, in excellent agreement with the direct measurement carried out on our TES detector using the same fitting technique discussed above, providing a substantially negligible dark count level $\gamma = (1,4 \pm 0,6) \times 10^{-6}$.

The same conclusion is obtained for any other model of the background, e.g. super-

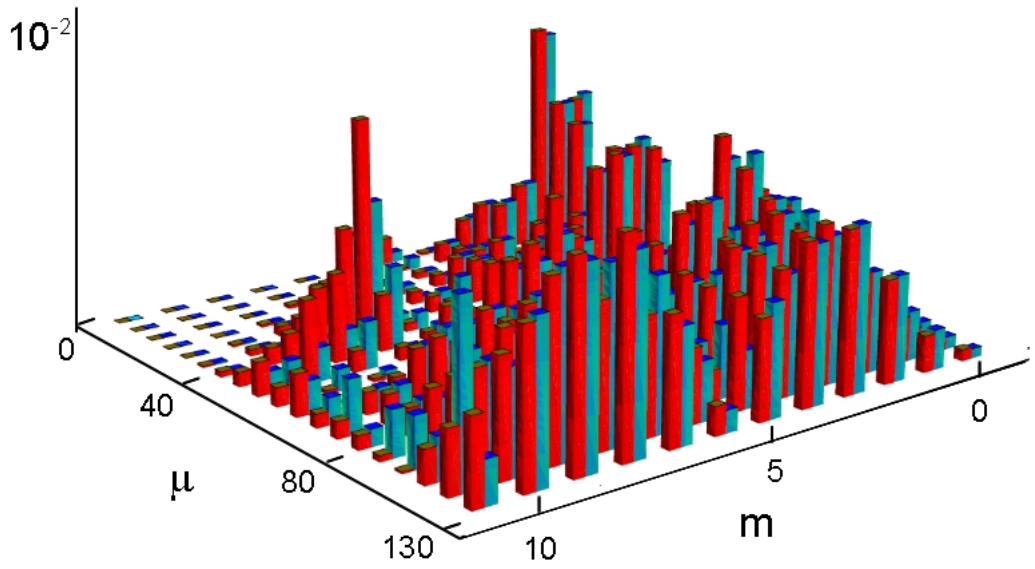

Figure 4.10: This graph shows the absolute differences between the $|p(n,j) - l(n,j)|$ (red left bars) and $|p(n,j) - r(n,j)|$ (light blue right bars). The differences are less of $10^(-2)$ in all the cases.

Poissonian.

The results of this experiment clearly validate the description of TES detectors as linear photon counters and, together with the precise estimation of the quantum efficiency, pave the way for practical applications of TES photon counters in quantum technology.

Chapter 5

Ancilla-asisted calibration of a measuring apparatus

A quantum measurement can be described by a set of matrices, one for each possible outcome, which represents the positive operator-valued measure (POVM) of the sensor. In the first section of this chapter, the theory of the first experimental POVM reconstruction that takes explicit advantage of a quantum resource (non-classical correlations with an ancillary state), is presented. In section 2, 3 and 4 is presented the experiment to reconstruct the POVM of a phase-insensitive photon-number-resolving detector by using strong quantum correlations of twin beams generated by PDC.

5.1 Quantum calibration of measurement devices

The calibration of a measuring apparatus, in a quantum mechanical description, corresponds to the knowledge of its POVM, i.e the form of the measurement operators $\hat{\Pi}_{(n)}$. An experimental method to extract the POVM of the apparatus under calibration is described in this section [65].

For an arbitrary input state the POVM of a measuring apparatus gives, via the Born

rule, the probability $p(n)$ of any measurement outcome n as:

$$p(n) = tr[\hat{\rho}\hat{\Pi}_{(n)}] \tag{5.1}$$

where $\hat{\rho}$ is the density operator of the state on the Hilbert space $\mathcal{H}$ of the system and the POVM is given by the set of operators $\{\hat{\Pi}_{(n)}\}$ on $\mathcal{H}$.

In Figure 5.1 the basic scheme of the experimental setup for a general quantum calibration is presented. A bipartite system is prepared in a predetermined state $\hat{R}$: one channel of the system is measured using the unknown apparatus A giving an outcome n, while in the other channel (described by the state $\hat{\rho}_{(n)}$) an observable $B^{(k)}$ from the quorum $\{B^{(k)}\}$ is measured by a tomographer, producing an output m. The combined outcome (n,m) is processed using a tomographic algorithm to obtain the POVM $\{\hat{\Pi}_{(n)}\}$ of the unknown apparatus.

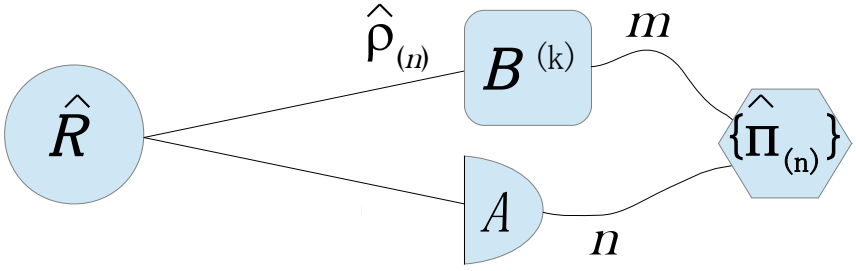

Figure 5.1: Scheme of the experimental setup used to determine the POVM of an unknown measurement apparatus A. A tomographer is used together with the device A on a bipartite system prepared in a predetermined state $\hat{R}$. An observable $B^{(k)}$ is measured from the quorum $\{B^{(k)}\}$ by the tomographer, giving an output m, while the unknown apparatus gives an output n. Using a tomographic algorithm, the joint outcomes (n,m) are processed to obtain the POVM $\{\hat{\Pi}_{(n)}\}$ of A.

The outcome (n,m) of the joint measurement is predicted to occur, by the Born rule (Eq. 5.1), with a probability:

$$p(n,m) = tr[(\hat{\Pi}_{(n)} \otimes |b_m\rangle \langle b_m|)\hat{R}] \tag{5.2}$$

where $\{|b_m\rangle\}$ is a fix observable at the tomographer, the generic bipartite state of the

two quantum systems is denoted by $\hat{R} = \sum_l |A_{(l)}\rangle\rangle\langle\langle A_{(l)}|$, and the POVM of the joint measurement is given by the tensor product of the individual POVM's. The joint probability $p(n, m)$ can be rewritten in terms of the conditional probability $p(m \mid n)$ via de Bayes's rule as

$$p(n, m) = p(n)p(m \mid n). \tag{5.3}$$

At the tomographer a convenient state $\hat{\rho}_{(n)}$, conditioned by the outcome n at the unknown measurement apparatus A, is introduced. Then, if Eqs. (5.1) and (5.3) are substituted in Eq. (5.2) the next result is obtained:

$$p(n, m) = p(n)tr[\hat{\rho}_{(n)} |b_m\rangle \langle b_m|] = tr[p(n)\hat{\rho}_{(n)} |b_m\rangle \langle b_m|]. \tag{5.4}$$

Expression (5.4) can be rewritten by evaluating the trace in two steps, i.e.:

$$p(n, m) = tr[|b_m\rangle \langle b_m| \, tr_1((\hat{\Pi}_{(n)} \otimes \mathbb{1})\hat{R})], \tag{5.5}$$

and by equalizing Eqs. (5.4) and (5.5) for any possible observable the following equality is obtained:

$$\hat{\rho}_{(n)}p(n) = tr_1((\hat{\Pi}_{(n)} \otimes \mathbb{1})\hat{R}). \tag{5.6}$$

If we introduce the map

$$\mathbb{R}(X) = tr_1((X \otimes \mathbb{1})\hat{R}) \tag{5.7}$$

where X is an operator on $\mathcal{H}$, the POVM element $\hat{\Pi}_{(n)}$ can be recovered from the conditioned state $\hat{\rho}_{(n)}$ by applying the inverse map $\mathbb{R}^{-1}$ as:

$$\hat{\Pi}_{(n)} = p(n)\mathbb{R}^{-1}(\hat{\rho}_{(n)}). \tag{5.8}$$

To recover the POVM element $\hat{\Pi}_{(n)}$, the input state $\hat{R}$ must be known, consequently

a precalibration stage is needed to determine it.

5.2 General Idea of the experiment

In this section, the general idea for the experimental reconstruction of a POVM is presented. The method takes advantage of a quantum resource, more specifically exploits non classical correlations with an ancillary state.

In our experiment, the device under test (DUT) is one of the fundamental components in quantum technology: a phase-insensitive photon-number-resolving (PNR) detector. The POVM elements of this detector are diagonal operators in the Fock basis and may be written as:

$$\widehat{\Pi}_{(n)} = \sum_m \Pi_{(n)m} \, |m\,\rangle\langle\, m| \tag{5.9}$$

with $\Pi_{(n)m}$ the probability of observing n counts when m photons impinge on the DUT, and the constraint that $\sum_n \Pi_{(n)m} = 1$.

The bipartite state that is used in our experiment is an optical twin beam with a state described by:

$$R = |R\,\rangle\rangle\langle\langle\, R| \tag{5.10}$$

with:

$$|R\rangle\rangle = \sum_i R_i |i\rangle|i\rangle \tag{5.11}$$

where $|i\rangle$ is the state of one beam with i photons and R_i is the probability amplitude of a particular state $|i\rangle$. The tomographer is an on-off detector with a selectable quantum efficiency η. The POVM of the tomographer is composed by the following operators:

$$\widehat{T}_{\rm no} = \sum_k (1-\eta)^k |k\rangle\langle k| \tag{5.12}$$

$$\widehat{T}_{yes} = \sum_k [1-(1-\eta)^k] |k\rangle\langle k| \tag{5.13}$$

where $\widehat{T}_{\rm no}$ corresponds to a *non-click* event (a non-photon detection) in the tomographer

and $\widehat{T}_{\rm yes}$ corresponds to a *click* event (detection) in the same channel.

According to Eq. (5.2), the joint probability of observing n photons on the DUT and having a *no-click* event in the tomographer is given by:

$$p(n,\mathrm{no}) = tr\left[\left(\widehat{\Pi}_{(n)} \otimes \widehat{T}_{\rm no}\right)|R\rangle\rangle\langle\langle R|\right]. \tag{5.14}$$

When put in explicit form, the trace becomes:

$$p(n,\mathrm{no}) = \sum_{l,s}\langle l|\otimes\langle s|\left[\left(\sum_m \Pi_{(n)m}|m\rangle\langle m|\right)\otimes\left(\sum_k (1-\eta)^k|k\rangle\langle k|\right)\cdot \right.$$
$$\left.\cdot\left(\sum_i R_i R_i^*|i\rangle\langle i|\otimes|i\rangle\langle i|\right)\right]|l\rangle\otimes|s\rangle$$

and then:

$$\begin{aligned} p(n,\mathrm{no}) &= \sum_{l,s}\sum_{m,k,i}\Pi_{(n)m}(1-\eta)^k\,|R_i|^2\,\cancel{\langle l|m\rangle}^{\delta_{lm}}\cancel{\langle m|i\rangle}^{\delta_{mi}}\cancel{\langle i|l\rangle}^{\delta_{il}}\otimes\cancel{\langle s|k\rangle}^{\delta_{sk}}\cancel{\langle k|i\rangle}^{\delta_{ki}}\cancel{\langle i|s\rangle}^{\delta_{is}} \\ &= \sum_m \Pi_{(n)m}(1-\eta)^m\,|R_m|^2 \end{aligned} \tag{5.15}$$

Analogously, the joint probability of observing n photons on the DUT and having a *click* event in the tomographer is

$$p(n,\mathrm{yes}) = \sum_m \Pi_{(n)m}[1-(1-\eta)^m]\,|R_m|^2\,. \tag{5.16}$$

The unknown elements $\Pi_{(n)m}$ are recovered by inverting the relations (5.15) and (5.16), once the $|R_m|^2$ elements have been determined.

We extract those elements by reconstructing the photon number distribution of the beam addressed to the tomographer (identical to its twin that is sent to the DUT). For this purpose, we exploit a least squares method based on the collection (at different tomographer's efficiencies) of the unconditional no-click events [73]:

$$p(\text{no}) = \sum_m |R_m|^2 (1-\eta)^m. \tag{5.17}$$

It is important to highlight that, with respect to the full quantum tomography [74–78], in this procedure no additional calibration is needed to determine the coefficients $|R_m|^2$ except for the calibration of the efficiencies of the tomographer.

5.3 POVM reconstruction of a tree detector

In this section, an experiment to reconstruct the POVM of a PNR detector based in a tree of single photon detectors is presented. An article based on this experiment is published in Physical Review Letters, reference [79].

5.3.1 Optical setup

The experimental setup is shown in Fig. 5.2. A pulsed Ti-Sapphire laser at 800 nm with a repetition rate of 76 MHz is duplicated via second harmonic generation to 400 nm. A 10 mm long nonlinear lithium iodate($LiIO_3$) crystal is pumped by the ultraviolet beam to produce non collinear type-I PDC, and degenerate twin beams (800 nm) are selected. One of the generated beams is sent to the tomographer, while the other is addressed to the DUT.

The tomographer is composed by a calcite polarizer, a 800 nm interference filter with 20 nm bandwith, a lens to couple the light into a multimode fiber and a fiber coupled silicon single-photon avalanche diode (SPAD). Because in both arms the down-converted photons have the same linear polarization, a variable attenuation is obtained by rotating the polarizer, varying the tomographer efficiency.

On the DUT arm, the PDC beam is filtered using an interference filter similar to that used in the tomographer (20 nm FWHM at 800 nm), coupled to a multimode fiber and delivered to the detector. The DUT is a detector tree composed by a 50:50 fiber beam splitter whose outputs are connected to two Si-SPADs. This tree detector can give three different outcomes corresponding to the detection of 0, 1, and 2 or more photons

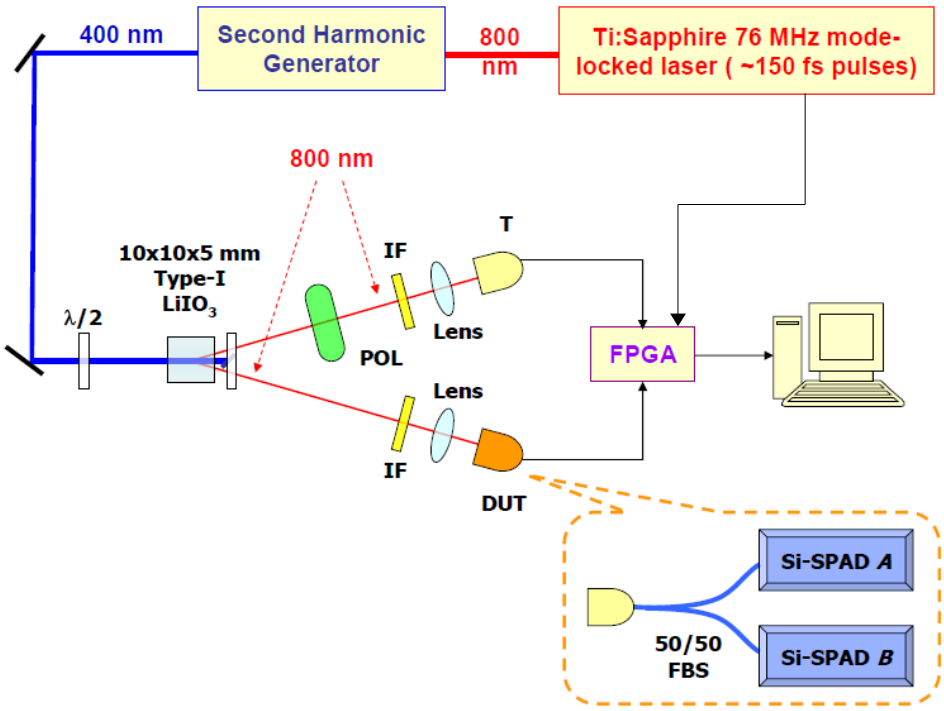

Figure 5.2: Experimental setup: A 800 nm Ti-Sapphire mode-locked laser is doubled via second harmonic generation to 400 nm and sent to a $LiIO_3$ crystal, generating type-I PDC. A half-waveplate ($\lambda \setminus 2$) is placed before the crystal to control the PDC generation by rotating the polarization. Correlated beams are selected: one is sent to the tomographer (T) and the other to the DUT. A linear polarizer (POL) is mounted in the T-path to allow the efficiency tuning. Interference filters (IF) with 20 nm FWHM are used to limit out-of-band light on the detectors. In both channels, a lens is used to couple the light to a multimode fiber. Two Si-SPADs connected through a 50:50 fiber beam splitter (FBS) constitute the PNR DUT to be characterized. The trigger pulse of the laser and the output signal of the three detectors are sent to a A for a real-time signal processing and data acquisition.

per laser pulse. An event 0 occurs when neither of the SPADs click, while an event 1 takes place when either SPAD click, but not both. An event 2 corresponds to the click of both SPADs.

The two Si-SPADs outputs of the PNR detector, the output of the tomographer detector (another Si-SPAD) and the laser trigger, are sent together to a Field Programmable Gate Array (FPGA) based precessing and data collection system.

5.3.2 Coincidence electronics

A Field Programmable Gate Array (FPGA) is the core of the coincidence electronics of this experiment. A scheme of the circuit programmed in the FPGA board is shown in Figure 5.3. The laser trigger output pulse is used as an external clock for the FPGA. If any of the three detectors gives a click signal in correspondence of a clock signal, the system discards any following event for a time interval corresponding to the dead time of the last detector clicking. In this way, the system allow to take data only if the three detectors are ready, ignoring the events affected by the dead time of the Si-SPADs.

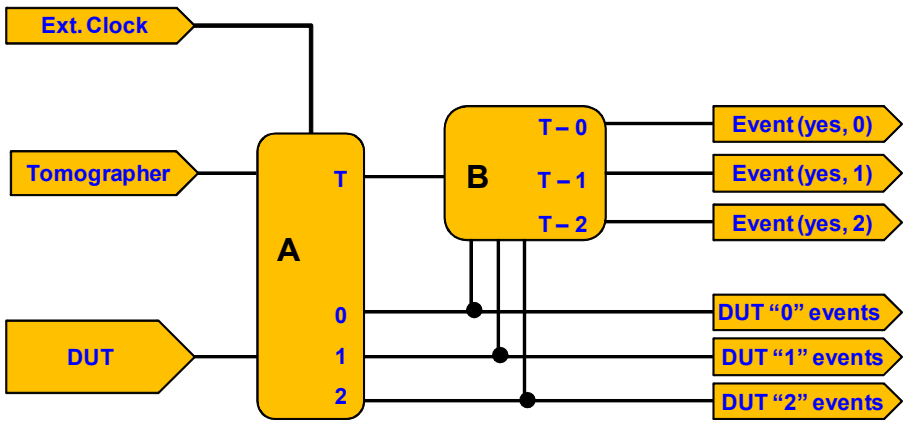

Figure 5.3: Scheme of the FPGA circuit. The external clock (Ext.Clock) is given by the laser trigger. Module A input are the signal of the tomographer's detector and the signal of the DUT (i.e. the signal of the two detectors of the PNRD). The circuit allows collection data only if the three detectors of the experiment are "alive" (i.e. are not in their dead time). Module A gives an output T when an event is registered in the tomographer's detector, and outputs 0, 1, and 2 correspond to the three outcomes of the PNR detector. Module B is a coincidence circuit between the T signal and the outputs 0, 1 and 2 of module A. The circuit gives 6 different outputs: the three outputs of the unconditional events in the PNR detector (DUT "0" events, DUT "1" events, and DUT "2" events), and the conditional events to have an outcome 0, 1 or 2 in the PNR detector and a click in the tomographer ("Event (yes, 0)", "Event (yes, 1)" and "Event (yes, 2)" respectively).

In module A the outputs of the tree detector are analyzed, providing three possible outputs: "0" when neither of the two detector clicks, "1" when only one of the detectors clicks, and "2" when both detectors click (corresponding to "DUT "0" events", "DUT "1" events", and "DUT "2" events" respectively, in Figure 5.3). This three outputs are

then used as input signals of module B. A fourth output (T) is present on module A, corresponding to a click signal from the tomographer's detector. This output is sent to module B to be analyzed.

Module B analyzes the correlations between T and the 0, 1, and 2 output signal of module A. The three outputs of module B are the events correspondig to a click in the tomographer and 0, 1 or 2 in the tree detector ("Event (yes, 0)", "Event (yes, 1)" and "Event (yes, 2)" respectively respectively in Figure 5.3).

A more detailed scheme of the FPGA circuit can be seen in Figure 5.4

By adding the unconditional events "DUT "0" events", "DUT "1" events", and "DUT "2" events", the number of total events is obtained and, together with the conditional outputs of module B, the probability to have 0, 1 or 2 event in the DUT when a *click* in the tomographer occurs, and the probability to have a 0, 1 or 2 event when there is *no-click* in the tomographer are obtained.

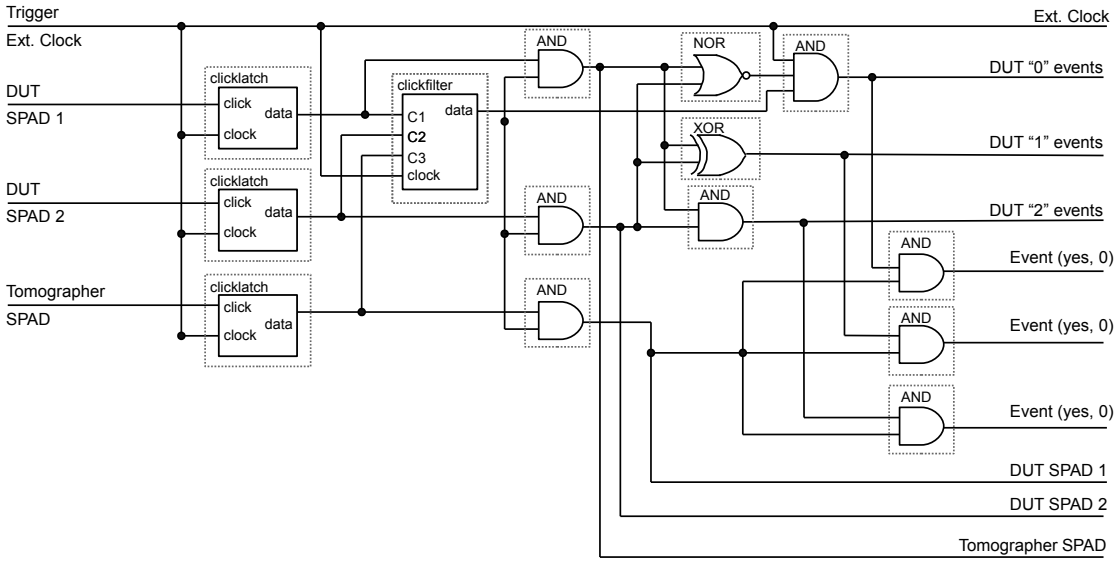

Figure 5.4: Detail of the FPGA circuit. The four input signals for the circuit, corresponding to the 3 detectors and the external clock (Ext. Clock), are represented in the right part of the scheme. The FPGA give ten different outputs, corresponding to the six output detailed in the scheme of Figure 5.3, the Ext. Clock and three extra output providing the coincidence counts between the Trigger and each detector. This three extra output are useful to monitor the experiment parameters.

5.3.3 Detectors and tomographer calibration

Before the data acquisition, we provide the calibration of the two SPADs of the PNR DUT (whose efficiencies are needed to calculate the expected POVM to be compared with the reconstruction result) and of the tomographer detector. The three Si-SPADs detectors are calibrated exploiting the Klyshko's method introduced in the Chapter 2 of this thesis. On Table 5.1 the quantum efficiency of the detectors are shown.

Table 5.1: Using Klyshko's method, the three detectors of the experiment are calibrated. The efficiency of the tomographer's detector (η_T) and the efficiency of the Si-SPAD A (η_A) and Si-SPAD B (η_B) are shown in this table.

	Efficiency	Uncertainty
Tomographer's detector	10,83 %	0,04 %
DUT's detector A	6,778 %	0,05 %
DUT's detector B	6,218 %	0,05 %

To provide different system efficiencies, the tomography arm polarizer is calibrated. The attenuation of the beam is measured for different angles of the polarizer, as seen in Figure 5.5.

To obtain the total efficiency of the tomographer's arm, the attenuation of the polarizer must be multiplied by the efficiency of the tomographer detector. In Figure 5.6, the graph of efficiency versus polarizer angle is shown.

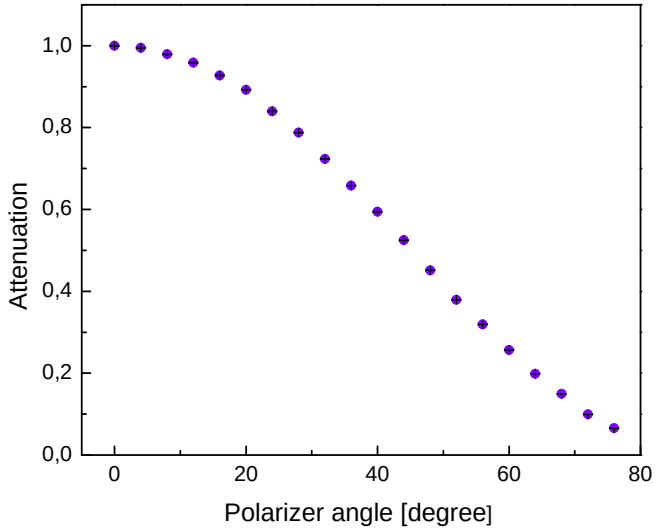

Figure 5.5: Attenuation of the beam in the tomographer arm vs the polarizer for twenty different angles.

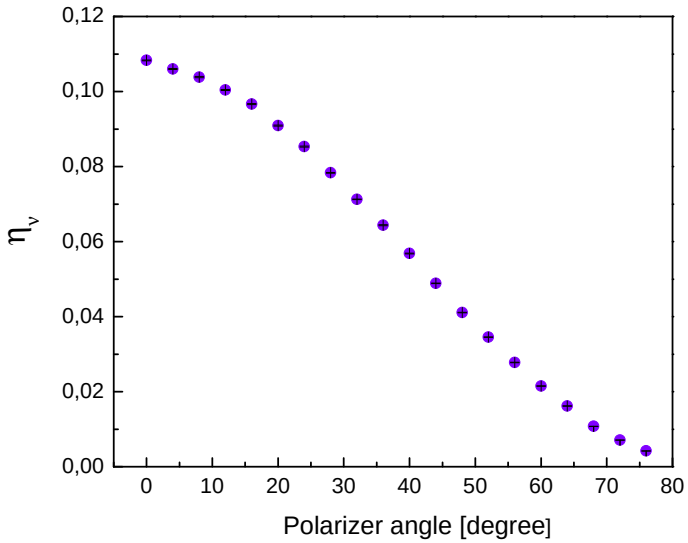

Figure 5.6: Efficiency of the tomographer (η_ν) vs the polarizer angle.

5.4 Results

Looking at each of the twin beams separately, the photon statistics of a single mode of PDC light is purely thermal. As the amount of contributing modes increase, like in our experimental conditions, the photon number distribution change from a thermal towards a Poissonian distribution [80, 81].

A first step in the reconstruction of the DUT's POVM is to determine the relative probabilities $f(0)$, $f(1)$ and $f(2)$, corresponding to the probability to have 0-, 1-, 2-clicks events respectively in the output of the tree detector. The expected probability to have no-click in our PNR DUT can be written as

$$f(0) = \sum_{m,n}^{\infty} \frac{e^{-\mu}}{m!n!} \left(\frac{\mu}{2}\right)^{m+n} (1-\eta_A)^m (1-\eta_B)^n \tag{5.18}$$

where a Poissonian distribution for the beam impinging on the DUT is assumed, where μ is the mean number of photons per pulse, m (n) is the number of photons in the output A (B) of the beam splitter, η_A (η_B) the efficiency of detector A (B). By solving Eq. (5.18) the following expression for $f(0)$ is obtained:

$$f(0) = e^{-\frac{1}{2}(\eta_A+\eta_B)\mu} \tag{5.19}$$

In analogy, the probabilities $f(1)$ and $f(2)$ are calculated, obtaining:

$$\begin{aligned} f(1) &= \sum_{m,n}^{\infty} \frac{e^{-\mu}}{m!n!} \left(\frac{\mu}{2}\right)^{m+n} [(1-\eta_A)^m (1-(1-\eta_B)^n) + (1-\eta_B)^n (1-(1-\eta_A)^m)] \\ &= e^{-\frac{1}{2}\eta_A\mu} + e^{-\frac{1}{2}\eta_B\mu} - 2e^{-\frac{1}{2}(\eta_A+\eta_B)\mu} \end{aligned} \tag{5.20}$$

$$\begin{aligned} f(2) &= 1 - f(0) - f(1) \\ &= e^{-\frac{1}{2}(\eta_A+\eta_B)\mu} \left(-1 + e^{\frac{1}{2}\eta_A\mu}\right) \left(-1 + e^{\frac{1}{2}\eta_B\mu}\right) \end{aligned} \tag{5.21}$$

In addition, for each efficiency η_ν of the tomographer, the relative probabilities of condi-

tional events paired with the tomographer's clicks $(f_{\eta_\nu}(yes,0),\ f_{\eta_\nu}(yes,1),\ f_{\eta_\nu}(yes,2))$ are determined as follows:

$$\begin{aligned} f_{\eta_\nu}(yes,0) &= \sum_{m,n}^{\infty} \frac{e^{-\mu}}{m!n!}\left(\frac{\mu}{2}\right)^{m+n}(1-\eta_A)^m(1-\eta_B)^n(1-(1-\eta_\nu)^{m+n}) \\ &= -e^{-\frac{1}{2}(\eta_A+\eta_B)\mu}\left(-1+e^{\frac{1}{2}(-2+\eta_A+\eta_B)\eta_\nu\mu}\right) \end{aligned} \tag{5.22}$$

$$\begin{aligned} f_{\eta_\nu}(yes,1) &= \sum_{m,n}^{\infty} \frac{e^{-\mu}}{m!n!}\left(\frac{\mu}{2}\right)^{m+n}[(1-\eta_A)^m(1-(1-\eta_B)^n)+ \\ &\quad +(1-\eta_B)^n(1-(1-\eta_A)^m)](1-(1-\eta_\nu)^{m+n}) \end{aligned} \tag{5.23}$$

$$\begin{aligned} &= e^{-\frac{1}{2}\eta_A\mu}+e^{-\frac{1}{2}\eta_B\mu}-2e^{-\frac{1}{2}(\eta_A+\eta_b)\mu}+2e^{\frac{1}{2}(-2+(-2+\eta_A+\eta_B)(-1+\eta_\nu))\mu}- \\ &\quad -e^{\frac{1}{2}(\eta_A(-1+\eta_\nu)-2\eta_\nu)\mu}-e^{\frac{1}{2}(\eta_B(-1+\eta_\nu)-2\eta_\nu)\mu} \end{aligned} \tag{5.24}$$

$$\begin{aligned} f_{\eta_\nu}(yes,2) &= \sum_{m,n}^{\infty} \frac{e^{-\mu}}{m!n!}\left(\frac{\mu}{2}\right)^{m+n}(1-(1-\eta_A)^m)(1-(1-\eta_B)^n)(1-(1-\eta_\nu)^{m+n}) \\ &= e^{-(\eta_A+\eta_B+\eta_\nu)\mu}\left(-e^{(\eta_A+\eta_B)\mu}-e^{\frac{1}{2}(\eta_A+\eta_B)(1+\eta_\nu)\mu}+e^{(\eta_A+\eta_B+\eta_\nu)\mu}+\right. \\ &\quad +e^{\frac{1}{2}(\eta_A+\eta_B+2\eta_\nu)\mu}+e^{\frac{1}{2}(\eta_A+2\eta_B+\eta_A\eta_\nu)\mu}+e^{\frac{1}{2}(2\eta_A+\eta_B+\eta_B\eta_\nu)\mu}- \\ &\quad \left.-e^{\frac{1}{2}(\eta_A+2\eta_B+2\eta_\nu)\mu}-e^{\frac{1}{2}(2\eta_A+\eta_B+2\eta_\nu)\mu}\right). \end{aligned} \tag{5.25}$$

The probability of "yes" events for each tomographer efficiency η_ν is obtained by adding up all the conditional probabilities

$$f_{\eta_\nu}(yes) = f_{\eta_\nu}(yes,0)+f_{\eta_\nu}(yes,1)+f_{\eta_\nu}(yes,2) = \ 1-e^{-\eta_\nu\mu} \tag{5.26}$$

The relative probabilities of conditional events corresponding to no-click events on the tomographer, are also determined:

$$
\begin{aligned}
f_{\eta_\nu}(no,0) &= \sum_{m,n}^{\infty} \frac{e^{-\mu}}{m!n!} \left(\frac{\mu}{2}\right)^{m+n} (1-\eta_A)^m (1-\eta_B)^n (1-\eta_\nu)^{m+n} \\
&= e^{\frac{1}{2}(-2+(2+\eta_A+\eta_B)(-1+\eta_\nu))\mu} \qquad (5.27)
\end{aligned}
$$

$$
\begin{aligned}
f_{\eta_\nu}(no,1) &= \sum_{m,n}^{\infty} \frac{e^{-\mu}}{m!n!} \left(\frac{\mu}{2}\right)^{m+n} [(1-\eta_A)^m (1-(1-\eta_B)^n) + \\
&\quad +(1-\eta_B)^n (1-(1-\eta_A)^m)](1-\eta_\nu)^{m+n} \\
&= -2e^{\frac{1}{2}(-2+(-2+\eta_A+\eta_B)(-1+\eta_\nu))\mu} + e^{\frac{1}{2}(\eta_A(-1+\eta_\nu)-2\eta_\nu)\mu} \\
&\quad +e^{\frac{1}{2}(\eta_B(-1+\eta_\nu)-2\eta_\nu)\mu} \qquad (5.28)
\end{aligned}
$$

$$
\begin{aligned}
f_{\eta_\nu}(no,2) &= \sum_{m,n}^{\infty} \frac{e^{-\mu}}{m!n!} \left(\frac{\mu}{2}\right)^{m+n} (1-(1-\eta_A)^m)(1-(1-\eta_B)^n)(1-\eta_\nu)^{m+n} \\
&= -e^{-\eta_\nu \mu} \Big(-1 + e^{\frac{1}{2}\eta_A(-1+\eta_\nu)\mu} + e^{\frac{1}{2}\eta_B(-1+\eta_\nu)\mu} - \\
&\quad -e^{\frac{1}{2}(\eta_A+\eta_B)(-1+\eta_\nu)\mu}\Big). \qquad (5.29)
\end{aligned}
$$

For each efficiency η_ν in the tomographer, the probability of "no" events is obtained by adding up all the conditional probabilities

$$
f_{\eta_\nu}(no) = f_{\eta_\nu}(no,0) + f_{\eta_\nu}(no,1) + f_{\eta_\nu}(no,2) = e^{-\eta_\nu \mu}. \qquad (5.30)
$$

As mentioned before, the reconstruction of the photon number distribution $|R_m|^2$ of the bipartite state, is a necessary preliminary step to obtain the POVM of the DUT. The $|R_m|^2$ elements are extracted exploiting the no-click probability of the tomographer $f(no)$.

In the experiment, 300 measurements of 1 second are realized for each of the 20 calibrated efficiencies in the tomographer. In Figure 5.7, logarithm of the unconditioned probability to have a no-click in the tomographer detector ($p(no)$) is plotted vs the efficiency of the tomographer (η_ν). The best fit of the data points is a Poisson distribution

with $\mu = 0{,}5983 \pm 0{,}0017$ mean photons per pulse.

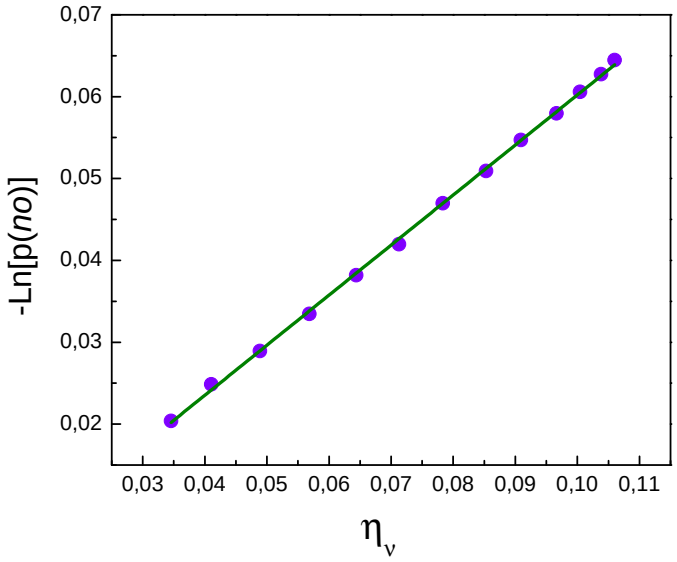

Figure 5.7: A linearized Poisson distribution with respect to detection efficiency. The best fit (line) of the $p(no)$ data (points) yields a Poisson distribution with $\mu = 0,5983 \pm 0,0017$ mean photons per pulse.

The $|R_m|^2$ elements are obtained by minimizing the following square difference

$$\sum_{\nu} \left[p_{\eta_\nu}^{exp}(no) - p_{\eta_\nu}(no)\right]^2 = \sum_{\nu} \left[p_{\eta_\nu}^{exp}(no) - \sum_{m} \left[|R_m|^2 (1-\eta_\nu)^m\right]\right]^2 \tag{5.31}$$

where $p_{\eta_\nu}^{exp}(no)$ is the experimental unconditional tomographer no-click event and the second term comes from Eq. (5.17).

In Figure 5.8 the experimentally reconstructed photon distribution is compared with the Poisson distribution with average photon number per pulse $\mu = 0{,}5983 \pm 0{,}0017$, as obtained from the fit of Figure 5.7. The experimentally reconstructed photon distribution is in excellent agreement with the Poisson distribution, with a fidelity larger than 99.4%, where the conventional definition of fidelity is used [73]. In our experiment the probability of observing more than 5 photons per pulse is negligible (less than 4 x

10^{-4}), that is why data are shown only up to $m = 5$ photons. The reconstruction is performed on 30 different data sets, the uncertainty bars in the histogram represent the 1σ variation of the reconstructions.

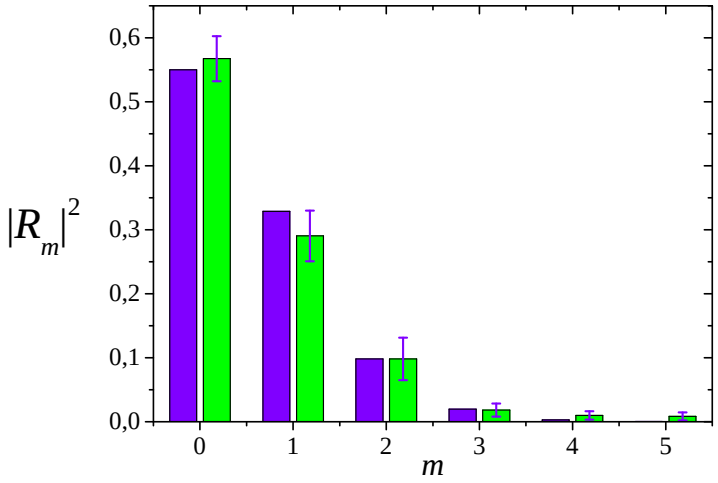

Figure 5.8: In this histogram, reconstructed bipartite state distribution $|R_m|^2$ (green bars) are compared to a Poisson distribution (violet bars) with the photon mean photon number per pulsed determined by the fit in Figure 5.7. Since in this experiment the probability of observing 5 or more photons per pulse is negligible, data are shown only up to $m = 5$ photons. The uncertainties represent the 1σ variations in the reconstructions performed on 30 different data sets.

The reconstructed $|R_m|^2$ and the calibrated efficiencies η_ν are substituted on Eqs. (5.15) and (5.16) to reconstruct the quantities Π_{nm}. To minimize the deviation between the measured and theoretical values of the probabilities, a regularized lest-square method [64, 69] is used. In particular, for each output n of the DUT and for each efficiency η_ν of the tomographer, the deviation between the observed $p^{exp}_{\eta_\nu}(n, yes)$ and the theoretical probabilities $p(n, yes)$ is minimized, as well as the deviation between $p^{exp}_{\eta_\nu}(n, no)$ and $p(n, no)$.

In Figure 5.9 the reconstructed $\Pi_0 m$, $\Pi_1 m$ and $\Pi_2 m$ are presented (respectively in plots a, b and c) for input photons up to $m = 5$. The excellent agreement between experimental and theoretical results is supported by the low uncertainties and fidelities

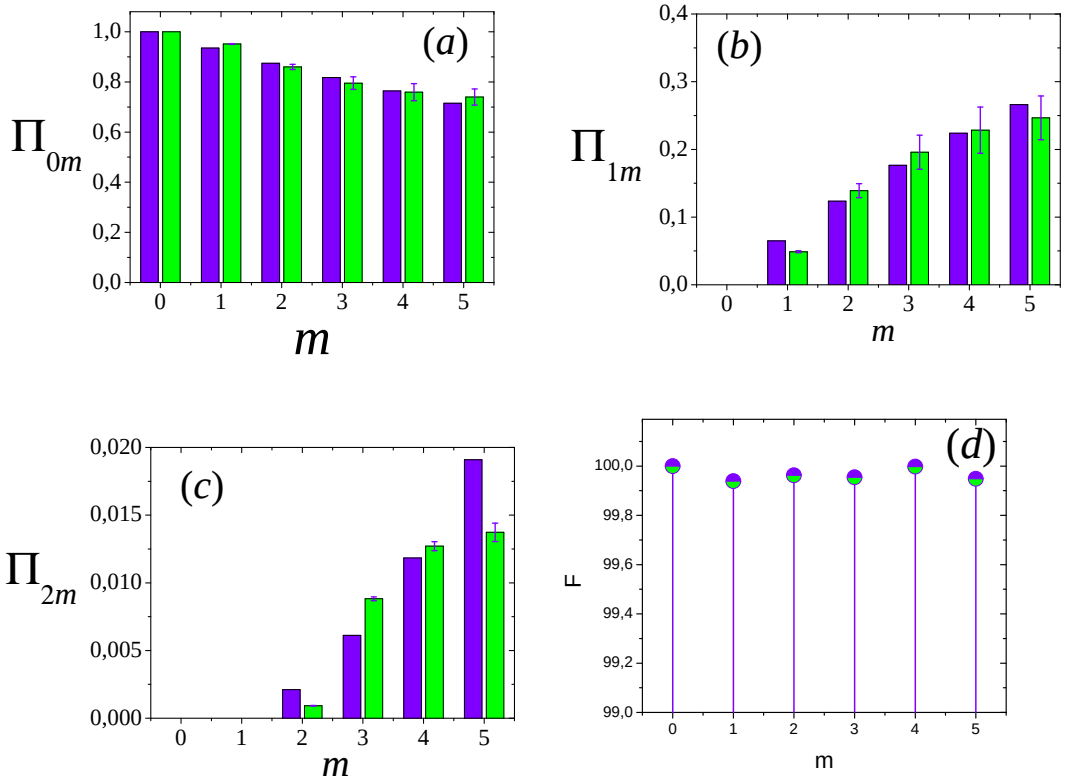

Figure 5.9: Reconstruction of the POVM elements up to $m = 5$. Theoretical histograms are shown in violet, experimentally reconstructed histograms are shown in green for: (a) Π_{0m}, (b) Π_{1m} and (c) Π_{2m}. The uncertainty bars represent the statistical fluctuations in the reconstructions performed on 30 different data sets. (d) Fidelity of the reconstructed POVM entries (with respect to the theoretical model) for each m. For elements with $m < 5$, the quality of the POVM elements reconstruction is independently confirmed by observed fidelities above 99.9%. For input states with $m \geq 5$, the accuracy starts deteriorating.

larger than $99,9\%$ for the first five valued values ($m \leq 4$). In inset (d) of Figure 5.9 the fidelities of the reconstructed POVM elements shown in Figure 5.9 are reported: the high values obtained confirm that the extracted POVM provides a reliability quantum description of the detector process. The quality of the POVM reconstruction rapidly decreases for $m \geq 5$ because of the lack of high photon number events, as discussed in connection with Figure 5.8. We want to highlight that this limitation is not inherent to our calibration method: in practice, the estimation of the probabilities with sufficient accuracy in the photon number range of interest, requires a bipartite state with enough Fock states in that range. Our twin beam source produces enough states up to $m = 4$.

Moreover, to further confirm the reliability of the reconstruction, in Figure 5.10 we compared the measured probabilities $p^{exp}_{\eta_\nu}(n, no)$ and $p^{exp}_{\eta_\nu}(n, yes)$, with the ones obtained from Eqs. (5.15) and (5.16) using the POVM and the reconstructed state. The near-unity fidelities, confirm that the reconstructed POVM provides reliable quantum description of the detection process of our PNR DUT.

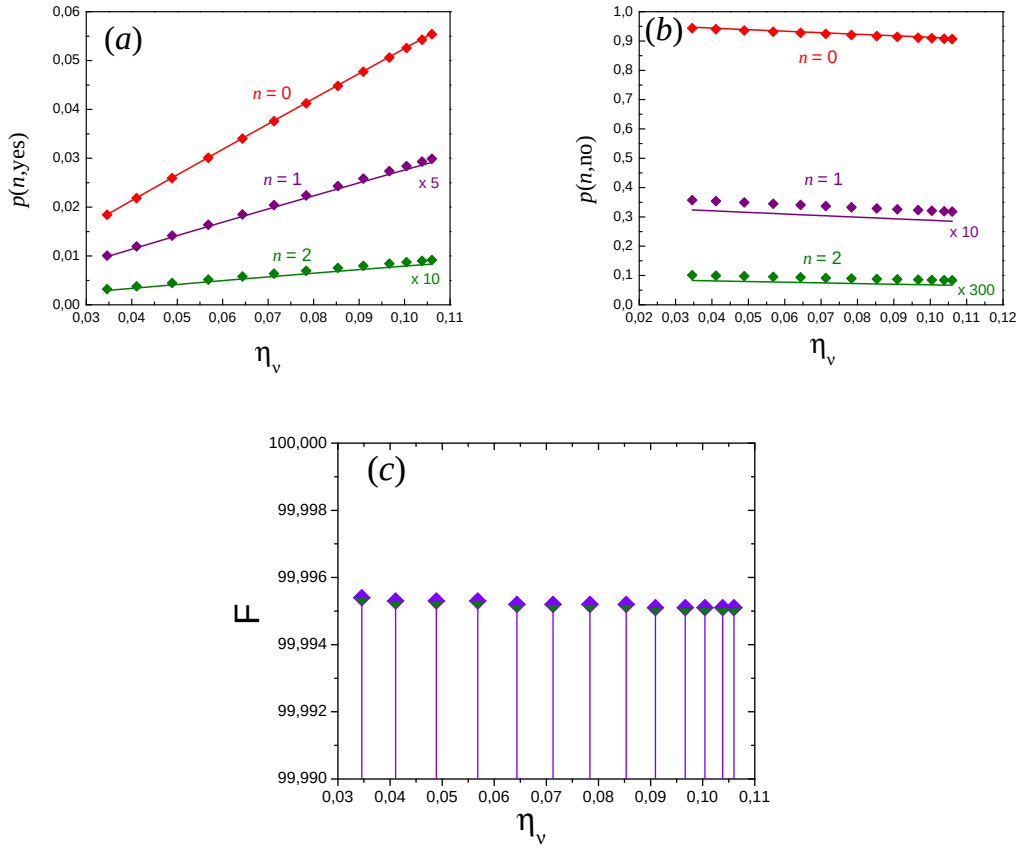

Figure 5.10: Comparison between theoretical (lines) and experimental (points) probabilities to (a) $p(n, yes)$ and (b)$p(n, no)$, for $n = 0{,}1$ and 2, for each measurement η_ν. In panel (a), probabilities for $n = 1$ and 2 are scaled by 5 and 10 respectively, while in panel (b) this quantities are scaled by 10 and 300 respectively. By substituting the measured values of the efficiencies η_ν, the reconstructed POVM and the reconstructed $|R_m|^2$ into Eqs. (5.15) and (5.16), the theoretical probabilities are obtained. Panel (c) The agreement between the theory and the experimental data is demonstrated in terms of the fidelity (F) that is larger than $99,99\%$.

Acknowledgements

I would like to thank the staff of Politecnico di Torino, Istituto Nazionale di Ricerca Metrologica and Instituto Nacional de Tecnología Industrial for the support and assistance throughout my PhD.

I want to thanks Dr. Giorgio Brida, for give me the opportunity to make my PhD at INRiM even though he didn't get to know me before.

Thanks Prof. Vittorio Penna, for being always available and interested in my work.

Many thanks to Dr. Ivo de Giovanni, who always gave me great advices and guided me both in experimental and theoretical aspects along my research work. Actually I will miss the long, looong talks with him.

I would like to specially acknowledge Dr. Fabrizio Piacentini, the researcher who most followed me in the daily work at the laboratory, for his suggestions and infinite patience. I really appreciate the time he dedicated to me in this years.

Thanks to Dr. Marco Genovese, for always being aware of my PhD progress.

I would also like to thank to: Richi and Chris, for introducing me to the quantum world; Karina and Héctor, for always give me support and encouragement; the whole Quantum Optics group at INRiM, for being my best teachers of Italian, and for always being willing to help me deal with typical situations of living in a new place; Michele, for being with me and sharing this long path; my family for always supporting me in my decisions; my friends, for giving me the opportunity to share a family atmosphere each time I needed.

Bibliography

[1] R. Daniel, R. Almog, A. Ron, S. Belkin, and Y. S. Diamand. Modeling and measurement of a whole-cell bioluminescent biosensor based on a single photon avalanche diode. *Biosens. Bioelectron.*, 24:882–887, 2008.

[2] X. Michalet, R. A. Colyer, J. Antelman, O. H. Siegmund, A. Tremsin, J. V. Vallerga, and S.Weiss. Single-quantum dot imaging with a photon counting camera. *Curr. Pharm. Biotechnol.*, 10:543–558, 2009.

[3] S. Felekyan, R. Kühnemuth, V. Kudryavtsev, C. Sandhagen, W. Becker, and C. A. M. Seidel. Full correlation from picoseconds to seconds by time-resolved and time-correlated single photon detection. *Rev. Sci. Instrum.*, 76:083104, 2005.

[4] M. Wahl, H.J. Rahn, I. Gregor, R. Erdmann, and J. Enderlein. Dead-time optimized time-correlated photon counting instrument with synchronized, independent timing channels. *Rev. Sci. Instrum.*, 78:033106, 2007.

[5] A. Pifferi, A. Torricelli, L. Spinelli, D. Contini, R.Cubeddu, F. Martelli, G. Zaccanti, A. Tosi, A. Dalla Mora, F. Zappa, and S. Cova. Time-resolved diffuse reflectance using small source-detector separation and fast single-photon gating. *Phys. Rev. Lett.*, 100:138101, 2008.

[6] M. Genovese. Research on hidden variable theories: A review of recent progresses. *Phys. Rep.*, 413:319–396, 2005.

[7] P. Traina, M. Gramegna, A. Avella, A. Cavanna, D. Carpentras, I. P. Degiovanni, G. Brida, , and M. Genovese. Review on recent groundbreaking experiments on quantum communication with orthogonal states. *Quantum Matter*, 2:153–166, 2013.

[8] V. Scarani, H. Bechmann-Pasquinucci, N. J. Cerf, M. Dušek, N. Lütkenhaus, and M. Peev. The security of practical quantum key distribution. *Rev. Mod. Phys.*, 81:1301, 2009.

[9] N. Gisin, G. Ribordy, W. Tittel, and H. Zbinden. Quantum cryptography. *Rev. Mod. Phys.*, 74:145, 2002.

[10] T. D. Ladd, F. Jelezko, R. Laflamme, Y. Nakamura, C. Monroe, and J. L. O'Brien10. Quantum computers. *Nature*, 464:45–53, 2010.

[11] P. Kok, M. J. Munro, K. Nemoto, T. C. Ralph, J. P. Dowling, and G. J. Milburn. Linear optical quantum computing with photonic qubits. *Rev. Mod. Phys.*, 79:135–174, 2007.

[12] J. C. Zwinkels, E. Ikonen, N. P. Fox, and M. L. Rastello. Photometry, radiometry and 'the candela': evolution in the classical and quantum world. *Metrologia*, 47:R15, 2010.

[13] V. Giovannetti, S. Lloyd, and L. Maccone. Advances in quantum metrology. *Nat. Phot.*, 5:222, 2011.

[14] P. Kumar, P. Kwiat, S.W. Nam A. Migdall, L. Vuckovic, and F. Wong . Photonic technologies for quantum information processing. *Quant. Inf. Proces.*, 3:215, 2004.

[15] S. Castelletto, I. P. Degiovanni, and M. L. Rastello. Theoretical aspects of photon number measurement. *Metrologia*, 37:613–616, 2000.

[16] J.Y. Cheung, C.J. Chunnilall, E.R.Woolliams, N.P.Fox, J.R.Mountford, J.Wang, and P.J. Thomas. The quantum candela: a re-definition of the standard units for optical radiation. *J. Mod. Opt.*, 54:373, 2007.

[17] G. Brida, S. Castelletto, C. Novero, and M. L. Rastello. Parametric amplification for radiance measurements. *Metrologia*, 35:247, 1998.

[18] Website address: www.quantumcandela.net.

[19] H. A. Bachor and T. C. Ralph. *A Guide to Experiments is Quantum Optics*. Wiley VCH, 2004.

[20] V. G. Dmitriev, G. G. Gurzadyan, and D. N. Nikogosyan. *Handbook of nonlinear optical crystals*. Springer-Verlag Berlin Heidelberg, 2nd edition, 1997.

[21] P. A. Franken et al. Generation of optical harmonics. *Phys. Rev. Lett.*, 7:118–119, 1961.

[22] E. Hendry, P. J. Hale, J. Moger, and A. K. Savchenko. Coherent nonlinear optical response of graphene. *Phys. Rev. Lett.*, 105:0974019, 2010.

[23] L. R. Dalton, A. W. Harper, R. Ghosn, W. H. Steier, M. Ziari, H. Fetterman, Y. Shi, R. V. Mustacich, A. K.-Y. Jen, and K. J. Shea. Synthesis and processing of improved organic second-order nonlinear optical materials for applications in photonics. *Chem. Mater.*, 7:1060–1081, 1995.

[24] J. M. Dudley and J. R. Taylor. Ten years of nonlinear optics in photonic crystal fibre. *Nature Photonics*, 3:85–90, 2009.

[25] Y. Mori, I. Kuroda, S. Nakajima, T. Sasaki, and S. Nakai. New nonlinear optical crystal: Cesium lithium borate. *App. Phys. Lett.*, 67:1818 – 1820, 1995.

[26] A. Fontcuberta i Morral and F. Stellacci. Light–matter interactions: Ultrastrong routes to new chemistry. *Nature Materials*, 11:272–273, 2012.

[27] E. Goulielmakis, M. Schultze, M. Hofstetter, V. S. Yakovlev, J. Gagnon, M. Uiberacker, A. L. Aquila, E. M. Gullikson, D. T. Attwood, R. Kienberger, F. Krausz, and U. Kleineberg. Single-cycle nonlinear optics. *Science*, 320:1614–1617, 2008.

[28] Y. Adachi, T. Yamamoto, M. Koashi, and N. Imoto. Simple and efficient quantum key distribution with parametric down-conversion. *Phys. Rev. Lett.*, 99:180503, 2007.

[29]

[30] V. Giovannetti, S. Lloyd, and L. Maccone. Advances in quantum metrology. *Nature Photonics*, 5:222–229, 2011.

[31] R. W. Boyd. *Non Linear Optics*. Academic Press, 3rd edition, 2008.

[32] N. Bloembergen. *Nonlinear Optics*. Benjamin, 1995.

[33] M. Fox. *Quantum Optics an introduction*. Oxford University Press, 2006.

[34] N. Boeuf et al. Calculating characteristics of non-collinear phase-matching in uniaxial and biaxial crystals. *Opt. Eng.*, 39:1016 – 1024, 2000.

[35] E. Hecht. *Optics*. Addison Wesley, 2002.

[36] M. O. Scully and M. S. Zubairy. *Quantum Optics*. Cambridge University, 1997.

[37] C. K. Hong and L. Mandel. Theory of parametric frequency down conversion of ligth. *Phys. Rev. A*, 31:2409–2418, 1985.

[38] M. H. Rubin, Y. H. Shid D. N. Klyshko, and A. V. Sergienko. Theory of two-photon entanglement in type-ii optical parametric down-conversion. *Phys. Rev. A*, 50:5122–5133, 1994.

[39] T: B. Pittman, D. V. Strekalov, D. N. Klyshko, M. H. Rubin, A. V. Sergienko, and Y. H. Shih. Two-photon geometric optics. *Phys. Rev. A*, 53:2804–2815, 1996.

[40] W. P. Wrice and I. A. Wamsley. Spectral information and distinguishability in type-ii down-conversion with a broadband pump. *Phys. Rev. A*, 56:1627–1634, 1997.

[41] L. Mandel and E. Wolf. *Optical coherence and quantum optics*. Cambridge University Press, 1995.

[42] D.N. Klyshko. *Photons and Nonlinear Optics*. Gordon and Breach Science Publishers, 1988.

[43] D. C. Burnham and D. L. Weinberg. Observation of simultaneity in parametric production of optical photon pairs. *Phys. Rev. Lett.*, 25:84 – 87, 1970.

[44] G. Brida, S. Castelletto, C. Novero, and M. L. Rastello. Measurement of the quantum efficiency of photodetectors by parametric fluorescence. *Metrologia*, 35:397 – 401, 1998.

[45] A. Migdall. Correlated-photon metrology without absolute standards. *Physics Today*, 52:41–46, 1999.

[46] A. Migdall. Absolute quantum efficiency measurements using correlated photons: Toward a measurement protocol. *IEEE Trans. on Instr. and Meas.*, 50:478–481, 2001.

[47] P. G. Kwiat, A. M. Steinberg, R. Y. Chiao, P. H. Eberhard, and M. D. Petroff. Absolute efficiency and time-response measurement of single-photon detectors. *Appl. Opt.*, 33:1844 – 1853, 1994.

[48] G. Brida, S. Castelletto, I. P. Degiovanni, C. Novero, and M. L. Rastello. Quantum efficiency and dead time of single-photons counting photodiodes: a comparison between two measurement techniques. *Metrologia*, 37:625–628, 2000.

[49] Website address: http://www.nist.gov/pml/div684/grp03/phasematching.cfm.

[50] Joint Committee for Guides in Metrology. Evaluation of measurement data — guide to the expression of uncertainty in measurement. *BIPM*, 2008.

[51] E. F. Zalewski and J. Geist. Silicon photodiode absolute spectral response self-calibration. *Appl. Opt.*, 19:1214–1216, 1980.

[52] S. V. Polyakov and A.L. Migdall. -high accuracy verification of a correlated-photon-based method for determining photocounting detection efficiency. *Optics Express*, 15:1390–1407, 2007.

[53] T. Kübarsepp and M. White. Ten-element photodetector for optical power and attenuation measurements. *Applied Optics*, 49:3774–3779, 2010.

[54] M. A. Nielsen and I. L. Chuang. *Quantum Computation and Quantum Information.* Cambridge, University Press, 2000.

[55] G. M. D'Ariano and P. Lo Presti. Quantum tomography for measuring experimentally the matrix elements of an arbitrary quantum operation. *Phys. Rev. Lett.*, 86:4195–4198, 2001.

[56] H.-K. Lo, S. Popescu, and T. Spiller, editors. *Introduction to Quantum Information and Computation.* World Scientific, 1998.

[57] G. M. D'Ariano, L. Maccone, and M. G. A. Paris. Orthogonality relations in quantum tomography. *Phys. Lett. A*, 276:25–30, 2000.

[58] G. M. D'Ariano, L. Maccone, and M. G. A. Paris. Quorum of observables for universal quantum estimation. *J. Phys. A*, 34:93, 2001.

[59] G. M. D'Ariano. Universal quantum estimation. *Phys. Lett. A*, 268:151–157, 2000.

[60] A. Feito, J. S. Lundeen, H. Coldenstrodt-Ronge, J. Eisert, M. B. Plenio, and I. A. Walmsley. Measuring measurement: theory and practice. *New J. Phys.*, 11:093038, 2009.

[61] J. Kim, S. Takeuchi, Y. Yamamoto, and H.H. Hogue. Multiphoton detection using visible light photon counter. *Appl. Phys. Lett.*, 74:902, 1999.

[62] D. Fukuda, G. Fujii, T. Numata, K. Amemiya, A. Yoshizawa, H. Tsuchida, H. Fujino, H. Ishii, T. Itatani, S.Inoue, and T. Zama. Titanium-based transition-edge photon number resolving detector with 98 *Opt. Expr.*, 19:870–875, 2011.

[63] B. Cabrera. Introduction to tes physics. *J. Low Temp. Phys.*, 151:82–93, 2008.

[64] G. Brida, L. Ciavarella, I.P. Degiovanni, Marco Genovese, L. Lolli, M.G. Mingolla, F. Piacentini, M. Rajteri, E. Taralli, and M.G.A. Paris. Quantum characterization of superconducting photon counters. *New J. Phys.*, 14:085001, 2012.

[65] G. M. D'Ariano, L. Marccone, and P. Lo Presti. Quantum calibration of measurement instrumentation. *Phys. Rev. Lett*, 93:250407, 2004.

[66] R Baltin. Sufficient conditions for convergence of antinormally ordered expansions of boson number operator functions $f(a\dagger a)$. *J. Phys. A: Math. Gen.*, 16:2721, 1983.

[67] M. G. A. Paris. Quantum state measurement by realistic heterodyne detection. *Phys. Rev. A*, 53:2658–2663, 1996.

[68] M. G. A. Paris. On density matrix reconstruction from measured distributions. *Opt. Commun.*, 124:277–282, 1996.

[69] J. S. Lundeen, A. Feito, H. Coldenstrodt-Ronge, K. L. Pregnell, Ch. Silberhorn, T. C. Ralph, J. Eisert, M. B. Plenio, and I. A. Walmsley. Tomography of quantum detectors. *Nature Phys.*, 5:27–30, 2009.

[70] C. Portesi, E. Taralli, R. Rocci, M. Rajteri, and E. Monticone. Fabrication of Ti/Au TESs for optical photon counting. *J. Low Temp. Phys.*, 151:261–265, 2008.

[71] E. Taralli, M. Rajteri, E. Monticone, and C. Portesi. Development of superconducting single-photon detectors at I.N.Ri.M. *Int. J. Quantum Inf.*, 5:293, 2008.

[72] D. Drung, C. Assmann, J. Beyer, A. Kirste, M. Peters, F. Ruede, and T. Schurig. Highly sensitive and easy-to-use squid sensors. *IEEE Trans. Appl. Supercond.)*, 17:699 – 704, 2007.

[73] G. Zambra, A. Andreoni, M. Bondani, M. Gramegna, M. Genovese, G. Brida, A. Rossi, and M. G. A. Paris. Experimental reconstruction of photon statistics without photon counting. *Phys. Rev. Lett*, 95:063602, 2005.

[74] G. M. D'Ariano, C. Macchiavello, and M. G. A. Paris. Detection of the density matrix through optical homodyne tomography without filtered back projection. *Phys. Rev. A*, 50:4298–4302, 1994.

[75] U. Leonhardta, M. Munroea, T. Kissb, T. Richterb, and M.G Raymera. Sampling of photon statistics and density matrix using homodyne detection. *Opt. Commun.*, 127:144–160, 1996.

[76] M. Asorey, P. Facchi, G. Florio, V.I. Man'ko, G. Marmo, S. Pascazio, and E.C.G. Sudarshan. Robustness of raw quantum tomography. *Phys. Lett. A*, 375:861, 2011.

[77] Yu. I. Bogdanov, G. Brida, M. Genovese, S. P. Kulik, E. V. Moreva, and A. P. Shurupov. Statistical estimation of the efficiency of quantum state tomography protocols. *Phys. Rev. Lett.*, 105:010404, 2010.

[78] M. Vasilyev, S. K. Choi, P. Kumar, and G. M. D'Ariano. Tomographic measurement of joint photon statistics of the twin-beam quantum state. *Phys. Rev. Lett.*, 84:2354–2357, 2000.

[79] G. Brida, L. Ciavarella, I. P. Degiovanni, M. Genovese, A. Migdall, M. G. Mingolla, M. G. A. Paris, F. Piacentini, and S. V. Polyakov. Ancilla-assisted calibration of a measuring apparatus. *Phys. Rev. Lett.*, 108:253601, 2012.

[80] S. Castelletto, I. P. Degiovanni, A. Migdall, V. Schettini, and M. Ware. Measurement of coupling pdc photon sources with single-mode and multimode optical fibers. *Proc. SPIE, Quantum Communications and Quantum Imaging II*, 5551:60, 2004.

[81] W. Helwig, W. Mauerer, and C. Silberhorn. Multimode states in decoy-based quantum-key-distribution protocols. *Phys. Rev. A*, 80:052326, 2009.